



## **A comparison of the ground magnetic responses during the 2013 and 2015 St. Patrick's Day geomagnetic storms**

**Xu, Z.; Hartinger, M. D.; Clauer, Robert C.; Peek, T.; Behlke, Rico**

*Published in:*  
Journal of Geophysical Research: Space Physics

*Link to article, DOI:*  
[10.1002/2016JA023338](https://doi.org/10.1002/2016JA023338)

*Publication date:*  
2017

*Document Version*  
Publisher's PDF, also known as Version of record

[Link back to DTU Orbit](#)

*Citation (APA):*  
Xu, Z., Hartinger, M. D., Clauer, R. C., Peek, T., & Behlke, R. (2017). A comparison of the ground magnetic responses during the 2013 and 2015 St. Patrick's Day geomagnetic storms. *Journal of Geophysical Research: Space Physics*, 122, 4023–4036. <https://doi.org/10.1002/2016JA023338>

---

### **General rights**

Copyright and moral rights for the publications made accessible in the public portal are retained by the authors and/or other copyright owners and it is a condition of accessing publications that users recognise and abide by the legal requirements associated with these rights.

- Users may download and print one copy of any publication from the public portal for the purpose of private study or research.
- You may not further distribute the material or use it for any profit-making activity or commercial gain
- You may freely distribute the URL identifying the publication in the public portal

If you believe that this document breaches copyright please contact us providing details, and we will remove access to the work immediately and investigate your claim.

## RESEARCH ARTICLE

10.1002/2016JA023338

## Special Section:

Geospace system responses to the St. Patrick's Day storms in 2013 and 2015

## Key Points:

- IMF  $B_z$  controls differing occurrences, durations, and intensities of several current systems between the two events
- Asymmetric ground magnetic field responses are observed at high-latitude regions in 2015 but not in 2013
- Differing MI system responses attributed primarily to differing solar wind driving conditions

## Correspondence to:

Z. Xu,  
z xu77@vt.edu

## Citation:

Xu, Z., M. D. Hartinger, C. R. Clauer, T. Peek, and R. Behlke (2017), A comparison of the ground magnetic responses during the 2013 and 2015 St. Patrick's Day geomagnetic storms, *J. Geophys. Res. Space Physics*, 122, 4023–4036, doi:10.1002/2016JA023338.

Received 15 AUG 2016

Accepted 1 MAR 2017

Accepted article online 10 MAR 2017

Published online 4 APR 2017

## A comparison of the ground magnetic responses during the 2013 and 2015 St. Patrick's Day geomagnetic storms

Z. Xu<sup>1</sup> , M. D. Hartinger<sup>1</sup> , C. R. Clauer<sup>1</sup> , T. Peek<sup>1</sup> , and R. Behlke<sup>2</sup> 
<sup>1</sup>Center for Space Science and Engineering Research, Virginia Tech, Blacksburg, Virginia, USA, <sup>2</sup>DTU Space, Technical University of Denmark, Kongens Lyngby, Denmark

**Abstract** The magnetosphere-ionosphere system response to extreme solar wind driving conditions depends on both the driving conditions and ionospheric conductivity. Since extreme driving conditions are rare, there are few opportunities to control for one parameter or another. The 17 March 2013 and 17 March 2015 geomagnetic storms driven by coronal mass ejections (CME) provide one such opportunity. The two events occur during the same solar illumination conditions; in particular, both occur near equinox on the same day of the year leading to similar ionospheric conductivity profiles. Moreover, both CMEs arrive at the same time of day leading to similar observing conditions (i.e., ground stations at similar magnetic local time in both events). We examine the ground magnetic response to each CME at a range of latitudes and in both the Northern and Southern Hemispheres, remote sensing several current systems. There are dramatic differences between the intensity, onset time and occurrence, duration, and spatial structure of the current systems in each case. For example, differing solar wind driving conditions lead to interhemispheric asymmetries in the high-latitude ground magnetic response during the 2015 storm; these asymmetries are not present in the 2013 storm.

## 1. Introduction

All geomagnetic storms involve an intensification of the ring current, usually represented by a decrease in the  $Dst$  or  $SYM-H$  index below a set threshold. Strong geomagnetic storms are often triggered by prolonged periods of southward interplanetary magnetic field (IMF) that occur during coronal mass ejection (CME) events [Gonzalez *et al.*, 1994]. There is considerable variety in the response of the magnetosphere-ionosphere (MI) system from storm to storm, including the intensity, onset time and occurrence, duration, and spatial structure of several large-scale current systems.

When the CME first arrives at the Earth, the magnetosphere is compressed, intensifying the Chapman-Ferraro currents. This intensification causes a sudden impulse, observed clearly at low-latitude ground magnetometer stations as an increase in the horizontal magnetic field [e.g., Russell *et al.*, 1994a]. During northward IMF conditions, the largest increase in the horizontal magnetic field (BH) is observed by ground magnetometers near the noon local time sector. Ground magnetometers at other local time sectors also observe increases in BH, but they are smaller. During southward IMF, the average increase in BH seen near noon is roughly 25% weaker when compared to northward IMF due to dayside reconnection, while the average increase in BH seen near midnight can be larger than increases seen during northward IMF. The increase in BH near midnight during southward IMF is caused by the occurrence of midlatitude bays associated with substorms [Russell *et al.*, 1994b].

During CME-driven geomagnetic storms, enhanced convection, substorm activity, and the buildup of the ring current are closely related to southward turnings of the north-south component of the IMF, hereafter referred to as IMF  $B_z$  (usually the  $z$  component refers to GSM coordinates), and dayside reconnection [Gonzalez *et al.*, 1994]. For example, IMF  $B_z$  is included in coupling functions describing how energy is transferred from the solar wind to the MI system, and such coupling functions have been used to predict substorm activity [e.g., Clauer, 1986; Chu *et al.*, 2014; McPherron and Chu, 2016], including the occurrence of the substorm current wedge (SCW). The SCW is a spatially localized feature—usually occurring near midnight—that can be seen clearly in magnetic local time (MLT)-UT diagrams constructed with magnetometer stations distributed in longitude [Clauer and McPherron, 1974; Clauer *et al.*, 2003]. Low- and middle-latitude ground magnetometer stations at longitudes within the SCW remote sense northward (toward magnetic pole) directed magnetic

perturbations [Clauer and McPherron, 1974; Kepko et al., 2015]. A recent study by Chu et al. [2014] used the inverse technique to calculate the width and location of the field-aligned currents. It provides a more quantitative analysis of the current system properties. The physical process of the buildup of the currents has been studied using numerical simulations, e.g., by Birn and Hesse [2013, 2014] and others.

The east-west component of the IMF, hereafter referred to as IMF  $B_y$ , also affects the structure of large-scale currents and magnetic field topology and the global ionospheric convection pattern during geomagnetic storms [Clauer, 1994]. Even moderate IMF  $B_y$  can distort the Earth's magnetic field. For example, nonzero IMF  $B_y$  twists magnetic field lines such that points in the Northern and Southern Hemispheres that nominally lie on the same magnetic field line (based on the Earth's intrinsic magnetic field) no longer do so; the effect increases with magnetic latitude [Ganushkina et al., 2013]. Other solar wind driving conditions also affect the structure of large-scale current systems and magnetic field topology, including solar wind dynamic pressure, solar wind velocity, and IMF  $B_z$  [Ganushkina et al., 2013].

Like the IMF, ionospheric conductivity is an important factor affecting large-scale current systems and the overall MI system response during CME storms. Large-scale current systems tend to close in regions of larger conductivity, and high-latitude currents are usually most intense in bands of enhanced conductivity caused by auroral precipitation—e.g., the westward electrojet and associated DP 1 and DP 2 current systems that occur during substorms [Clauer and Kamide, 1985]. The pattern of auroral precipitation, solar illumination, and ionospheric conductivity all change with season, leading to changes in the structure of large-scale current systems. Thus, identical solar wind driving conditions can produce different MI responses from season to season.

The 17 March 2013 and 17 March 2015 geomagnetic storms driven by CME provide a rare opportunity to isolate the effect of solar wind driving conditions on the MI system response. The two events occur during the same solar illumination conditions (both near equinox on the same day of the year) leading to similar ionospheric conductivity profiles, yet they are associated with very different IMF conditions. In this study, we examine the ground magnetic response to each CME at a range of latitudes and in both the Northern and Southern Hemispheres, remote sensing several current systems. As we shall show for these two storms, there are dramatic differences between the intensity, onset time and occurrence, duration, and spatial structure of the current systems related to IMF  $B_z$  and other solar wind driving conditions. In section 2, we describe the instruments used to analyze the ground magnetic response. In section 3, we present solar wind and ground magnetometer observations and discuss the differences between each event. In section 4, we discuss and summarize our results.

## 2. Data

In this study, we use multiple data sets to compare solar wind driving to the global MI system response: satellite observations in the solar wind, ground-based magnetometers, and ground-based radars. First, data from the NASA OMNI database (<http://omniweb.gsfc.nasa.gov>) are used to examine the solar wind driving conditions including the IMF. These data have been propagated from an upstream solar wind monitor to the Earth's bow shock (see King and Papitashvili [2004] for more details of the OMNI database).

Second, we obtain ground-based magnetometer data from multiple stations distributed globally to examine how the MI system response evolves both spatially and temporally during the CME events. High-latitude station data include Autonomous Adaptive Low-Power Instrument Platforms (AAL-PIP) from the Magnetosphere-Ionosphere Science Team (<http://mist.nianet.org/index.html>) [Clauer et al., 2014] and DTU Space stations (Denmark's National Space Institute, Technical University of Denmark). AAL-PIP stations on the East Antarctic Plateau lie on the same International Geomagnetic Reference Field (IGRF) as a Northern Hemisphere DTU Space station on the west coast of Greenland; these paired stations can thus be used for interhemispheric comparisons of the high-latitude ground magnetic response.

We also obtain low- and middle-latitude magnetometer station data using the SuperMAG database (<http://supermag.jhuapl.edu/>). SuperMAG collects data from many sources and processes them to be in a similar format [Gjerloev, 2012]. For this study, we selected stations that were as evenly distributed in longitude as possible to better examine the MLT-dependent MI system response during each CME event; these data will be used for MLT-UT plots described later in the paper. All magnetometer stations used in this study and their coordinates are listed in Table 1.

**Table 1.** The List of Ground-Based Geomagnetic Stations Used in This Study, Including 22 Middle- and Low-Latitude Stations and 18 High-Latitude Conjugate Stations<sup>a</sup>

Station Code	GeoLON	GeoLAT	MagLON	MagLAT	Station Location
<i>Middle- to Low-Latitude Stations</i>					
CLF	2.27	48.02	79.42	43.11	Chambon la foret
KIV	30.30	50.72	104.63	46.56	Kiev
AMS	77.57	−37.80	140.23	−48.87	Martin de Vivas
AAA	76.92	43.25	150.22	38.83	Alma Ata
CKI	96.84	−12.19	168.90	−22.26	Cocos-Keeling Islands
IRT	104.45	52.17	178.45	47.79	Irkoutsk
BMT	116.20	40.30	−170.01	34.69	Beijing Ming Tombs
KNY	130.88	31.42	−156.01	24.49	Kanoya
KAK	140.18	36.23	−147.05	29.12	Kakioka
MSR	142.27	44.37	−145.03	37.64	Moshiri
CTA	146.30	−20.10	−138.73	−28.92	Charters Towers
CNB	149.36	−35.32	−132.34	−45.03	Canberra
HON	202.00	21.32	−89.10	20.88	Honolulu
PPT	210.42	−17.57	−73.70	−16.22	Pamatai
FRN	240.30	37.10	−54.87	42.65	Fresno
BOU	254.77	40.13	−38.68	48.51	Boulder
BSL	270.37	30.35	−17.88	40.69	Bay St Louis
FRD	282.63	38.20	−0.64	48.05	Fredericksburg
SJG	293.85	18.11	11.85	26.75	San Juan
KOU	307.27	2.21	23.49	6.05	Kourou
VAL	349.75	51.93	70.41	49.13	Valentia
HAD	355.52	50.98	74.74	47.37	Hartland
<i>High-Latitude Conjugate Stations</i>					
PG0	88.68	−83.67	38.71	78.57	Antarctic
PG1	77.20	−84.50	41.22	75.99	Antarctic
PG2	57.96	−84.42	38.15	74.82	Antarctic
PG3	37.63	−84.81	37.09	73.54	Antarctic
PG4	12.25	−83.34	36.43	70.93	Antarctic
PG5	5.71	−81.96	37.12	69.49	Antarctic
THL	290.77	77.47	28.35	84.46	West Greenland
SVS	294.90	76.02	32.05	82.71	West Greenland
KUV	302.82	74.57	41.11	80.35	West Greenland
UPN	303.85	72.78	39.46	78.57	West Greenland
UMQ	307.87	70.68	41.87	75.97	West Greenland
GDH	306.47	69.25	38.72	74.83	West Greenland
ATU	306.43	67.93	37.56	73.56	West Greenland
STF	309.28	67.02	40.25	72.18	West Greenland
SKT	307.10	65.42	36.66	70.98	West Greenland
GHB	308.27	64.17	37.32	69.52	West Greenland
FHB	310.32	62.00	38.56	66.92	West Greenland
NAQ	314.56	61.16	42.68	65.22	West Greenland

<sup>a</sup>GeoLON/LAT stands for geographic longitude/latitude. MagLON/LAT stands for magnetic longitude/latitude.

Finally, we obtain global ionospheric convection maps derived from Super Dual Auroral Radar Network (SuperDARN) radar line of sight velocities. These are a standard higher-level data product obtained using the Virginia Tech SuperDARN website (<http://vt.superdarn.org/>).

### 3. Results

#### 3.1. Differences in the Solar Wind Driving Conditions

Both CME events examined in this study occurred on 17 March, near equinox. In both cases, the interplanetary shock arrived at the Earth at nearly the same time of day. In the context of understanding the global ground magnetic response, these two facts are very important. The solar zenith angle at each ground magnetometer station will be nearly the same when the shock arrives, and this makes it likely that local ionospheric conductivity will also be similar. Thus, most of the similarities and differences in the ground

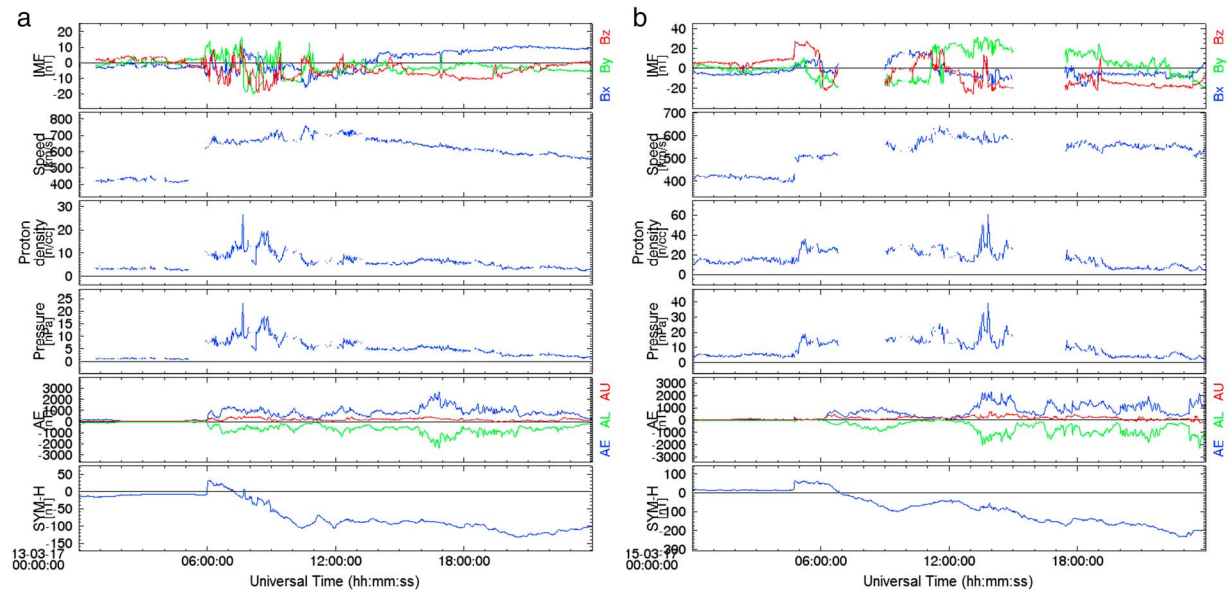


**Figure 1.** The solar wind conditions and geomagnetic activity indices from OMNI data on 17 March (a) 2013 and (b) 2015. From top to bottom in each panel, interplanetary magnetic field in GSM coordinates ( $x$  = blue,  $y$  = green, and  $z$  = red), solar wind flow speed, proton density, dynamic pressure, the AE/AL/AU indices (blue/green/red), and the SYM-H index.

magnetic response—and the MI system response—for these two events will be determined by the solar wind driving conditions.

With regard to solar wind driving conditions, there are several important differences between the two events: *Shock arrival time.* The first to fourth panels of Figures 1a and 1b are for solar wind (OMNI) magnetic field, flow speed, density, and dynamic pressure data that have all been propagated to the Earth's bow shock. In Figure 1a for the 2013 event, step-like changes in these parameters (IMF  $B_x$ ,  $B_y$ , and  $B_z$  (GSM coordinates), solar wind speed, and solar wind proton density) at 0600 UT indicate the shock arrival; for example, Figure 1a (fourth panel) indicates a step-like dynamic pressure increase associated with the interplanetary shock. The same parameters are shown in Figure 1b for the 2015 event; as before, step-like changes in these parameters indicate a shock arrival at 0445 UT. IMF  $B_z$ . As indicated by the red lines in the first panels of Figures 1a and 1b, the first southward turning of IMF  $B_z$  after the shock arrives is at ~0600 UT in both events. In the 2013 event this occurs almost immediately after the shock arrives, whereas in the 2015 event it is roughly 75 min later. Moreover, the duration and magnitude of the southward turnings differ between the two events. In 2013,  $B_z$  is southward on average throughout the main phase of the storm, mostly from 06 UT to 24 UT, but there are fluctuations with several northward turnings. In contrast, the 2015 event has more prolonged periods of purely southward (0600–0700 UT, 1230–1310 UT, and 1400–2400 UT) and purely northward (0450–0600 UT and 1030–1120 UT) IMF with larger magnitude (average near 20 nT amplitude) than the 2013 event (average near 10 nT), such as a prolonged period of strong southward  $B_z$  (–20 nT) beginning at 1200 UT. IMF  $B_y$ . As indicated by the green lines in the first panel of Figures 1a and 1b, the IMF  $B_y$  is relatively large in amplitude compared to other IMF components (20–30 nT of  $B_y$  comparing to 10–20 nT of  $B_x$  and  $B_z$ ) during several periods of the 2015 event, but it is rarely the largest component in the 2013 event. For example, during the periods 0600–0700 UT and 1000–1100 UT in the 2015 event, IMF  $B_y$  was –20 nT, and during 1100–1400 UT it was above 20 nT, becoming as large as 30 nT. In contrast, during the 2013 event, the IMF  $B_y$  fluctuated between –10 and 10 nT. *Other solar wind parameters.* Other solar wind parameters differ between the two events, though less substantially. On average, the solar wind flow speed is roughly 650 km/s during the 2013 storm compared to 600 km/s during the 2015 storm. Solar wind dynamic pressure remained close to or above 10 nPa for much of the 2015 storm in contrast to the 2013 storm where there were only a few periods near the beginning of the storm with dynamic pressure exceeding 10 nPa.

The timelines shown in Figure 2 summarize and compare the timing of the shock arrival and changes in IMF  $B_z$  between the two events.

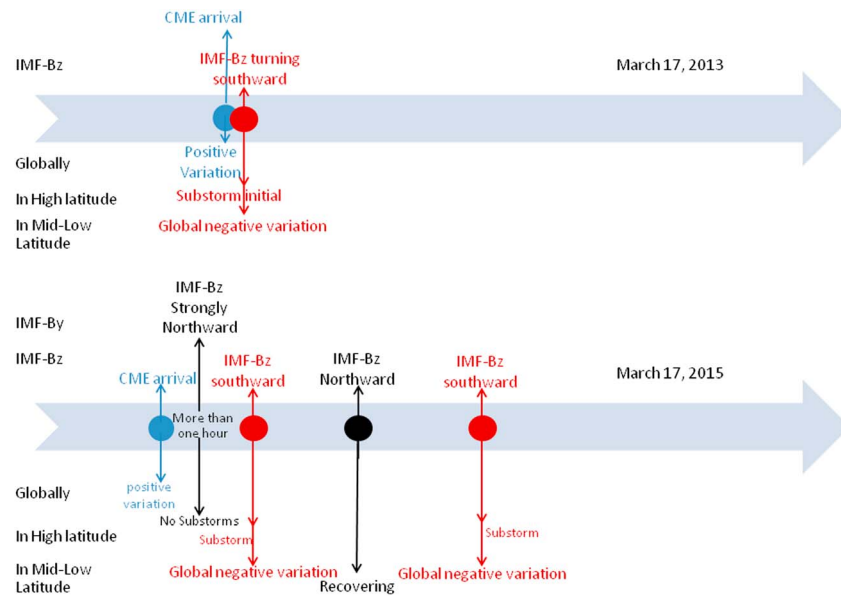


**Figure 2.** Timelines showing how the ground magnetic response varies according to solar wind driving conditions in the (top) 17 March 2013 event and (bottom) 17 March 2015 event.

### 3.2. Interhemispheric Differences in the High-Latitude MI Response

To test for the presence of interhemispheric differences in the high-latitude MI response, we compared the ground magnetic response at two high-latitude north-south chains of magnetometers at the same magnetic meridian: AAL-PIP stations on the East Antarctic Plateau and DTU Space stations on the west coast of Greenland. All Northern Hemisphere stations lie on the same IGRF magnetic field line (i.e., the Earth's unperturbed magnetic field) as a Southern Hemisphere station.

In the 2013 event, the geomagnetic field response to the CME was very similar in the Northern and Southern Hemispheres. Figure 3a shows the north-south (based on background magnetic field) magnetic perturbations measured at Northern Hemisphere stations (black lines) and nominally magnetically conjugate Southern Hemisphere stations (red lines). All stations are ordered according to magnetic latitude, from high to low (i.e., distance from polar cap increases from top to bottom of figure). In both the Northern (UMQ, GDH, and ATU) and Southern (PG1, PG2, and PG3) Hemispheres, negative magnetic perturbations begin at 0600 UT. The negative perturbations follow soon after the southward turning of the IMF and are likely related to the westward electrojet and substorm activity. This feature appears nearly identical in the Northern and Southern Hemispheres, in terms of timing and amplitude. In particular, the red and black lines in Figure 3a lie nearly on top of each other between 0600 and 0830 UT as the north-south component of the magnetic field ( $B_x$ ) first decreases then recovers to its initial value at three station pairs: UMQ and PG1, GDH and PG2, and ATU and PG3. Other smaller perturbations occurring throughout the day exhibit similar trends: there are no significant differences between high-latitude magnetic perturbations in the Northern and Southern Hemispheres.

As shown in Figure 3b (same format as 3a), the 2015 event exhibits much larger interhemispheric differences than the 2013 event during several periods. For example, at 0600 UT, there is a large positive magnetic perturbation seen in the Southern Hemisphere stations that is not seen in the Northern Hemisphere, indicating a current system that was either more intense or closer to the locations of the Southern Hemisphere stations. Another example occurs from 1100 to 1500 UT, when the Southern Hemisphere measurements appear completely different from the Northern Hemisphere: generally positive perturbations seen in the Northern Hemisphere and generally negative perturbations seen in the south, with the amplitudes varying with latitude and hemisphere.

Figure 4 provides further confirmation of these asymmetries and global context using ground-based SuperDARN radars. In particular, this figure shows ionospheric convection maps in the Northern



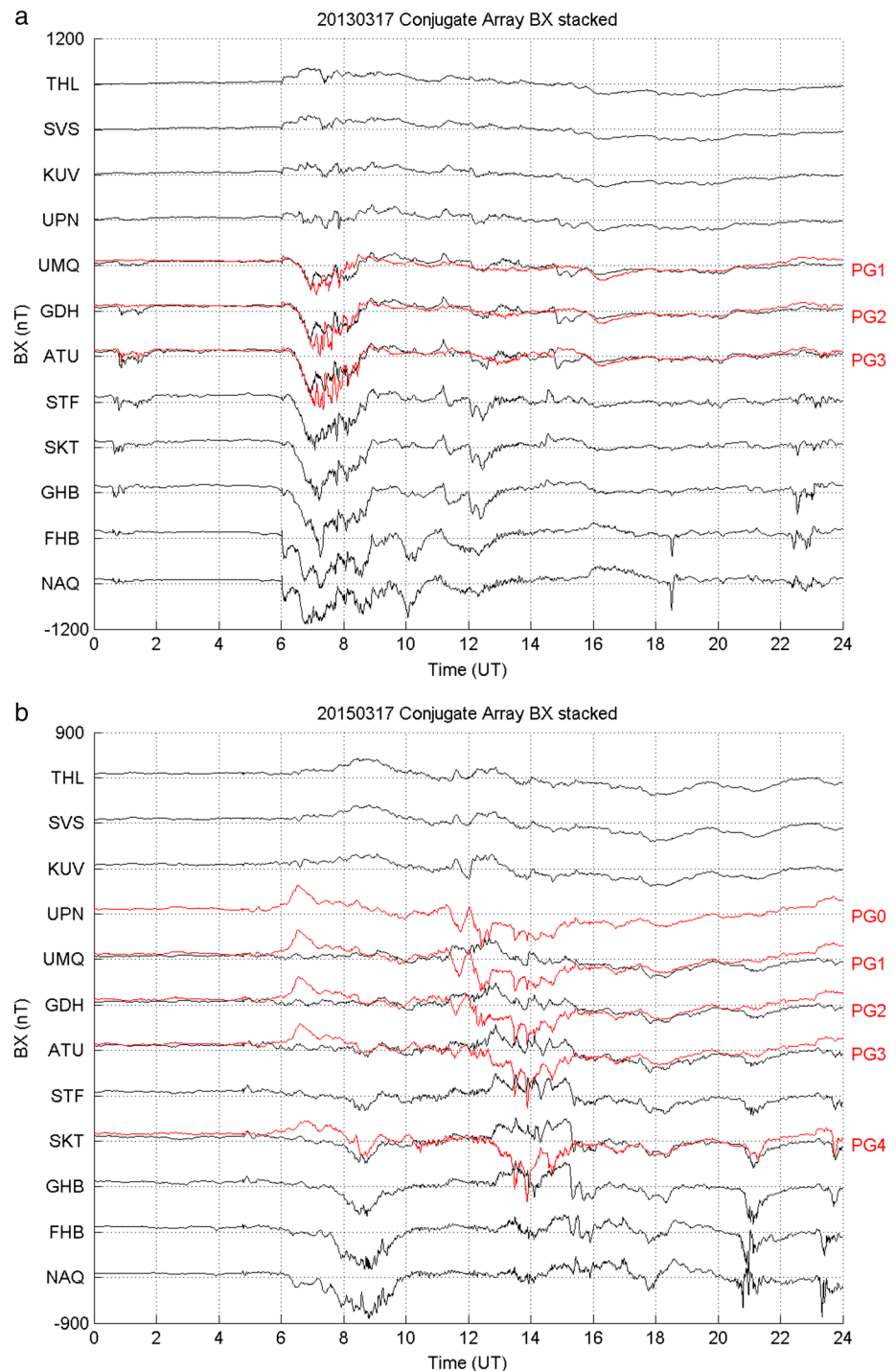


**Figure 3.** The north-south magnetic field variation from high-latitude magnetically conjugate stations on 17 March (a) 2013 and (b) 2015. Black lines and station labels are for the DTU Space Greenland stations, whereas red is for AAL-PIP Antarctica stations. Stations are ordered from top to bottom with increasing distance from their respective poles.

Hemisphere (top) and Southern Hemisphere (bottom) constructed using fits to line of sight velocities measured by the radars. On each plot, contours indicate lines of constant potential for the period 0628–0630 UT on 17 March 2015. The patterns shown are different than the standard two-cell convection pattern. The patterns shown in Figure 4 (top and bottom) are also asymmetric, consistent with north-south asymmetries in the global convection pattern, magnetic field topology, and large-scale currents. The

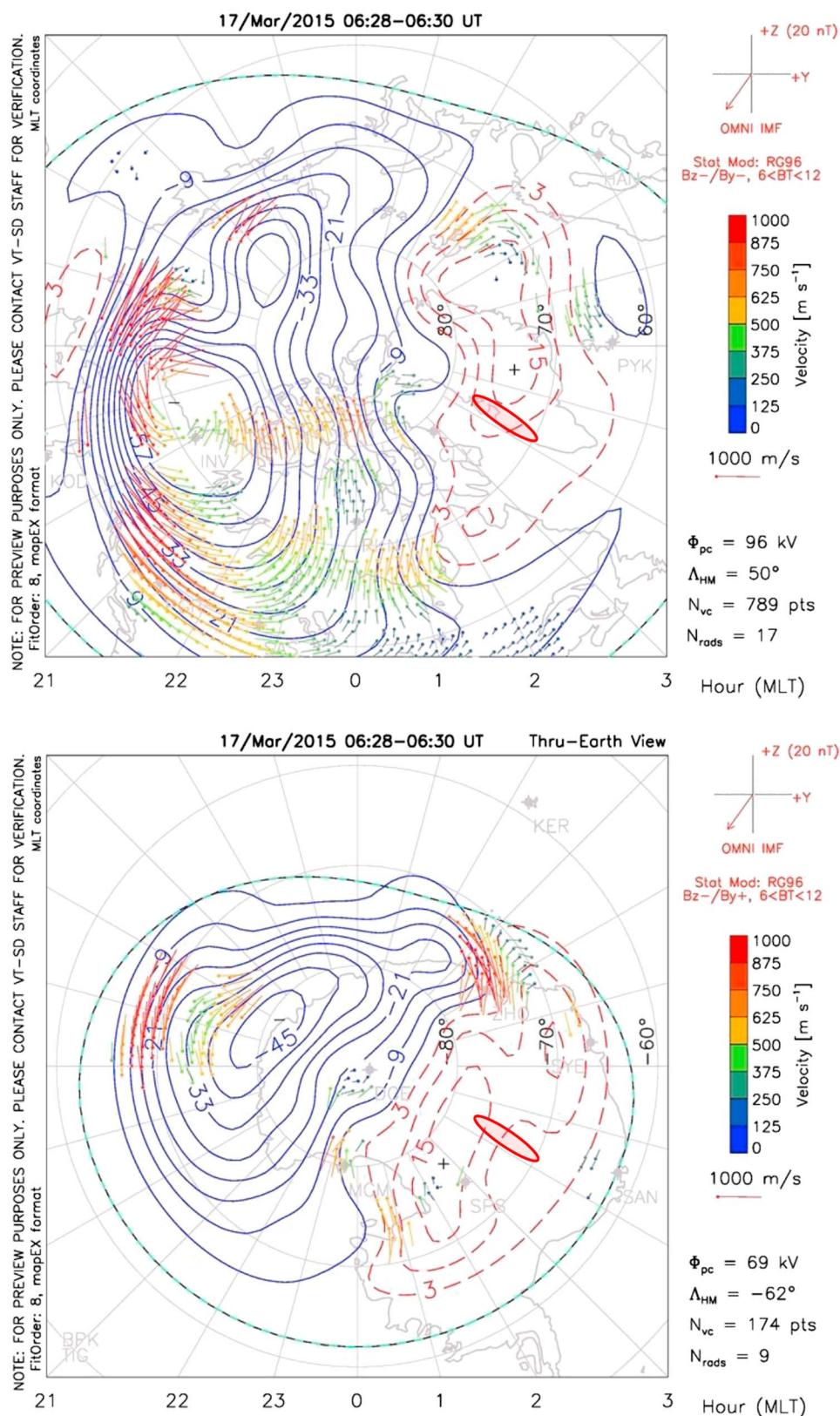


**Figure 4.** The ionospheric convection pattern derived from SuperDARN line of sight velocity measurements made between 0628 and 0630 UT on 17 March 2015 in the (top) Northern Hemisphere and (bottom) Southern Hemisphere. Red shadowed regions indicate the location of magnetometer stations in Greenland and Antarctica.



shaded red regions of Figure 4 indicate the location of high-latitude ground magnetometer stations used in this study; these are the locations where large asymmetries in the ground magnetic response were detected during these two events. The ground magnetometers complement the SuperDARN observations, providing observations of asymmetric current systems in regions with little radar coverage. Each measurement highlights the need for observations in both hemispheres to characterize potentially different or asymmetric responses.

### 3.3. Global Ground Magnetic Response in Middle- and Low-Latitude Regions

The *SYM-H* index displayed in the sixth panel of Figures 1a and 1b indicates more activity in the latter stages of the storm for the 2015 event (1b) in comparison to the 2013 event (1a), reaching values large as  $-200$  nT in 2015 in comparison to  $\sim -100$  nT in 2013. Moreover, *SYM-H* exhibits a double dip feature in the 2015 event that is not present in the 2013 event. Both of these differences can be traced back to the differences in IMF  $B_z$  in the two events; in 2015, IMF  $B_z$  tends to be larger in magnitude and there are two prolonged periods of southward IMF  $B_z$  with a period of northward IMF in between. This sequence of southward, northward, southward IMF  $B_z$  leads to a sequence of decreasing, increasing, and decreasing *SYM-H* (intensifying, weakening, and intensifying ring current).

Though *SYM-H* presents a useful proxy for the average ring current intensity, it does not provide global information about the MLT-dependent MI response during these two storms. Accordingly, we examine data from a global chain of low- and middle-latitude ground magnetometers distributed nearly uniformly in MLT. Figure 5 shows the north-south magnetic perturbation ( $B_x$ ) observed at 22 stations during 17 March 2013, ordered according to longitude or MLT. All stations observe a step-like increase in magnetic field associated with the arrival of the interplanetary shock; the shock compresses the dayside magnetopause, intensifying the Chapman-Ferraro currents and creating the positive perturbation seen on the ground that is usually strongest at stations near noon. Following the step-like increase, all stations see a gradual decrease associated with the gradual intensification of the ring current. This decrease follows the step-like increase almost immediately, likely due to the rapid southward turning of IMF  $B_z$  during this event. These perturbations are consistent with what is observed in the *SYM-H* index, but they also provide more information on the variation of the perturbations and currents as a function of longitude.

Figure 6 shows the same information as Figure 5 but for the 17 March 2015 event. As in 2013, there is a positive increase in the north-south magnetic field when the shock arrives at 0445 UT. However, the increase persists much longer than in 2013, 75 min until roughly 0600 UT (i.e., the square wave-like feature seen at many stations from  $\sim 0445$  to 0600 UT, as opposed to a more spike-like feature in 2013 at 0600 UT). This difference is consistent with the different solar wind drivers; in 2015, the IMF  $B_z$  did not turn southward until roughly 75 min after the shock arrived, at  $\sim 0600$  UT. Figure 6 also shows that the north-south magnetic perturbation decreases as the ring current intensifies, as in the 2013 event. However, unlike in 2013, the decrease is not monotonic; there are two periods of decreasing north-south magnetic field perturbation and corresponding increasing ring current intensity, the first at 0600 and the second at 1200 UT, consistent with the two extended periods of southward IMF  $B_z$  that are present in the 2015 event but not the 2013 event.

To more easily visualize the MLT-dependent ground magnetic response as a function of time, we next display MLT-UT magnetic disturbance maps using the middle- and low-latitude data shown in the stack plots. These maps are constructed using the following steps described more fully in Clauer *et al.* [2003]: (1) remove baseline from north-south magnetic field measurement using standard SuperMAG database procedure [Gjerloev, 2012], (2) normalize magnetic perturbation according to each station's magnetic latitude to remove latitudinal dependence of perturbation (and focus on MLT dependence), and (3) use interpolation and smoothing techniques to fill all 24 MLT bins at each UT time using each station's MLT.

Figure 7a shows 24 h in both MLT and UT, covering the entire day on 17 March 2013. The x axis is for UT, y axis is for MLT with midnight in the middle of the plot, and color indicates the perturbation amplitude (red for positive and blue for negative). Consistent with the stack plot in Figure 5, there is a large positive variation seen at all MLT at  $\sim 0600$  UT. Shortly after, a more localized positive perturbation is observed near local midnight, from  $\sim 0630$  to 0830 UT. This feature is related to the SCW [Clauer and McPherron, 1974]. Apart from this feature, negative perturbations are observed shortly after the initial compression of the magnetosphere at all MLT, related to the ring current intensification. Note that these maps provide only a rough estimate of the

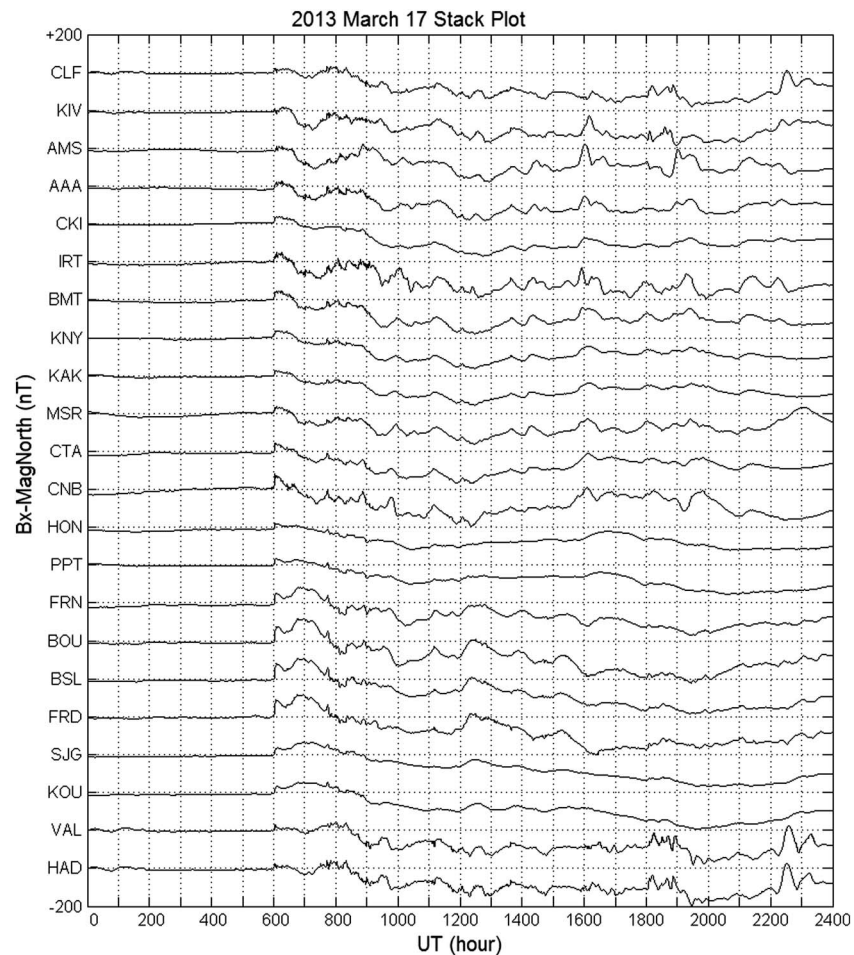


**Figure 5.** The north-south magnetic field perturbation observed at middle- and low-latitude ground magnetometer stations on 17 March 2013. The stations are ordered according to longitude, and each box is equal to 200 nT on the y axis and 1 h on the x axis.

location of the SCW; as shown by *Chu et al.* [2014] it is possible to more quantitatively estimate the central meridian of the SCW and width and location of associated field-aligned currents using an advanced inverse technique; we shall postpone this analysis to a future study, focusing instead on major differences between the 2013 and 2015 events (e.g., occurrence of SCW).

In the 2015 event shown in Figure 7b (same format as 7a), it is clear that the intensification of the Chapman-Ferraro current lasts longer than in 2013; in particular, positive perturbations (yellow colors) persist at all MLT from ~0445 to 0600 UT. Also, in contrast to the 2013 event, there is no localized positive perturbation (SCW) near midnight. Evidently, whatever conditions led to the SCW in the 2013 event did not occur during the 2015 event. Finally, this figure shows a local minimum in magnetic perturbation of ~100 nT from ~0900 to 1000 UT; as discussed previously, this is consistent with the two southward turnings of the IMF and decrease then increase then decrease sequence in *SYM-H*.

Figures 8a and 8b show finer details of the ground magnetic response in the first hour after the arrival of the CME. To construct this figure, the magnetic field measurement at 0600 UT and 0445 UT—the CME arrival times in each event, respectively—was used as a baseline and subtracted from all subsequent measurements in the following hour. Color indicates the perturbation amplitude after baseline subtraction, the x axis is for UT, and the y axis is for MLT with midnight at the center as before. The stations are assumed to remain fixed in MLT, so the data in each MLT bin come from the same station(s) for the entire interval. Data for the 17 March 2013 event are shown in Figure 8a; as before, the most prominent feature is the large positive disturbance during the latter part of the hour, strongest near midnight. This feature is absent in the 2015 event

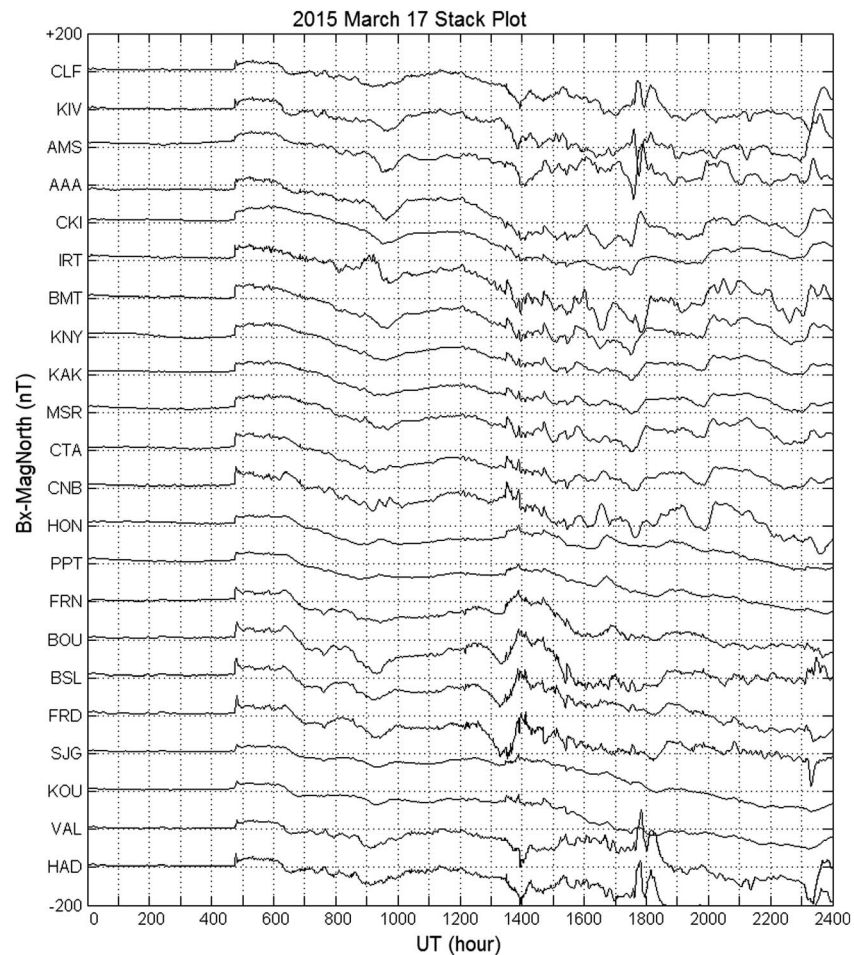


**Figure 6.** The north-south magnetic field perturbation observed at middle- and low-latitude ground magnetometer stations on 17 March 2015. The stations are ordered according to longitude, and each box is equal to 200 nT on the y axis and 1 h on the x axis.

shown in Figure 8b. When comparing these two figures, it is also clear how rapidly the ring current intensifies during the 2013 event (blue color seen in the second part of the interval shown in Figure 8a) in contrast to the 2015 event (no blue seen in 8b).

Finally, Figures 8a and 8b show a large, positive increase near midnight just after the arrival of the CME. In the 2013 event, this feature is more pronounced, but there is also an increase observed in the 2015 event. These features can be at least partially interpreted in the context of the *Russell et al.* [1994a, 1994b] studies. During northward IMF conditions, a CME compresses the dayside magnetosphere and intensifies the Chapman-Ferraro currents upon arriving at Earth. The intensified Chapman-Ferraro currents generate a positive horizontal magnetic perturbation that is largest at middle- to low-latitude ground stations near noon; ground stations at other local times observe similar perturbations with smaller amplitude [*Russell et al.*, 1994a]. During southward IMF conditions, there are two important differences from northward IMF: dayside reconnection and the occurrence of midlatitude bays associated with substorms triggered by the CME. The latter effect generates positive horizontal magnetic perturbations near midnight, and both effects combine to generate a different local time dependence for the horizontal magnetic perturbation associated with the CME: larger horizontal magnetic perturbations near midnight compared to noon [e.g., *Russell et al.*, 1994b, Figure 7]. However, with regard to the 2013 event, it is surprising for a midlatitude bay to occur almost instantly after the shock arrives (within 2–3 min). With regard to the 2015 event, it is surprising that the initial nightside response is comparable to the dayside response, despite this being a purely northward IMF condition. We shall leave a full explanation of the origin of these features for future work that includes comparisons with models and numerical simulation.



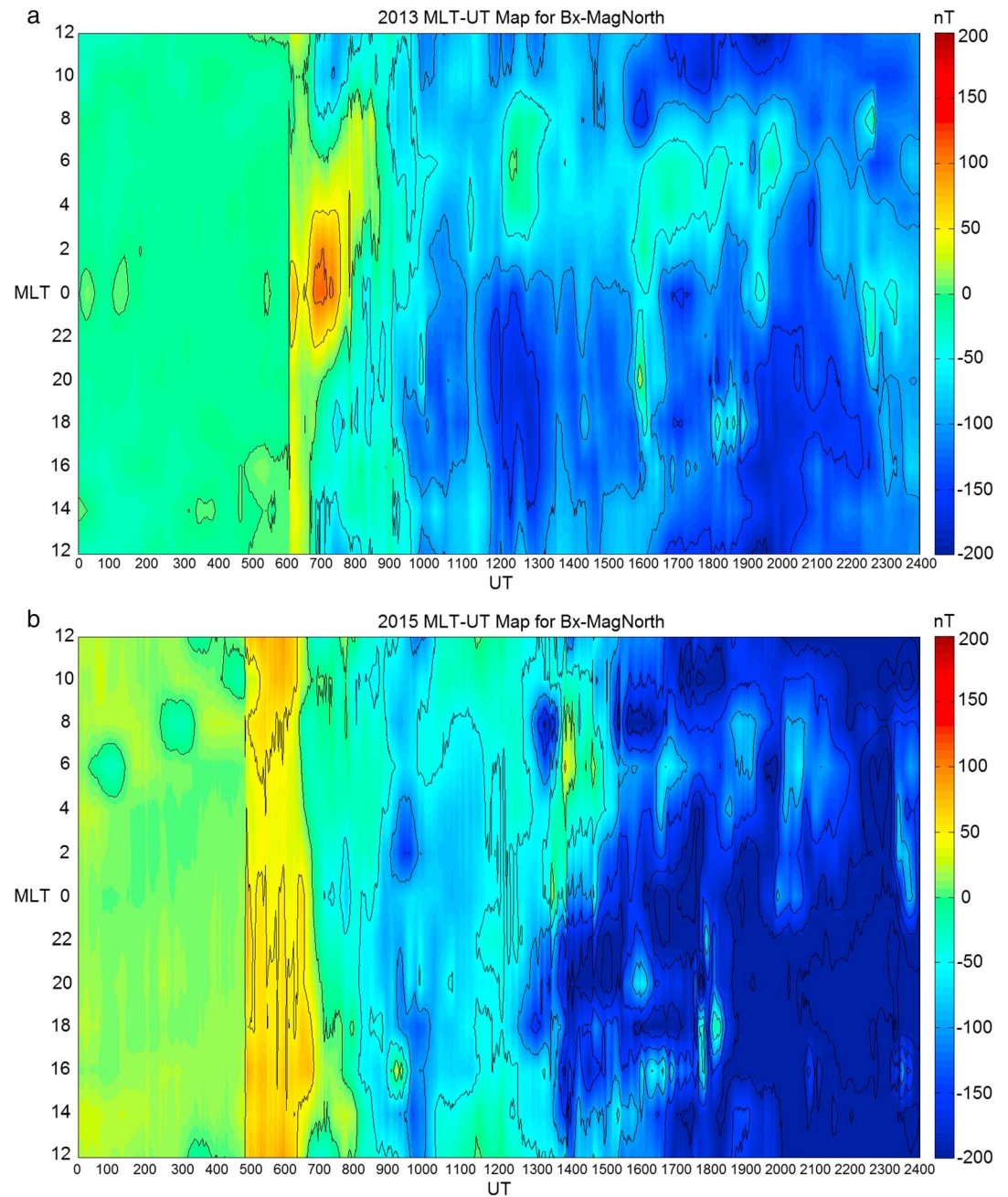


**Figure 7.** MLT-UT maps of the normalized north-south magnetic perturbation on 17 March (a) 2013 and (b) 2015. The x axis is for UT time, y is for MLT, and color indicates perturbation amplitude (red positive and blue negative). See text for full details of how these maps are constructed.

The timelines shown in Figure 2 summarize the features observed at low and midlatitude ground magnetometer stations and discussed in this section.

#### 4. Discussion and Summary

The results shown in the previous section are summarized in the timelines in Figure 2 that compare the solar wind conditions and ground magnetic responses in the 17 March 2013 and 17 March 2015 CME storm events. The two events have a few features in common with each other and other storm events, for example, the initial compression of the magnetosphere resulting in global positive north-south magnetic perturbation

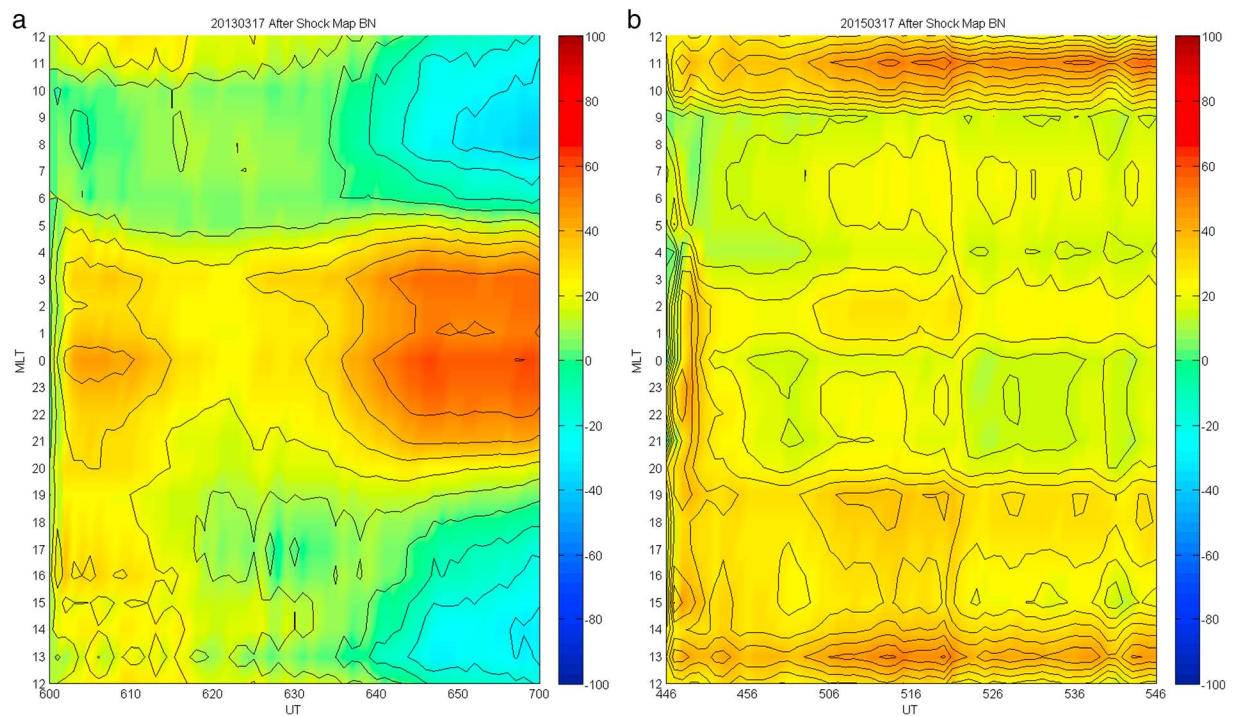


**Figure 8.** MLT-UT maps of the normalized north-south magnetic perturbation during the first hour after the CME arrives on 17 March (a) 2013 and (b) 2015. The x axis is for UT time, y is for MLT, and color indicates perturbation amplitude (red positive and blue negative). See text for full details of how these maps are constructed.

and decreasing north-south magnetic perturbation during the main phase of the storm associated with southward turnings in IMF  $B_z$ .

These timelines also demonstrate how strongly IMF  $B_z$  controls differing MI system responses in each storm event. The different times and durations of southward turnings in IMF  $B_z$  lead to very different MI responses: SCW in the beginning of the 2013 but not the 2015 event, rapid ring current intensification in 2013 but not 2015, two phase ring current intensification in 2015 but not 2013. Differing substorm activity, which itself is related to variations in IMF  $B_z$ , may also have led to differing ring current dynamics and, thus, differing storm evolutions (single phase in 2013 and two phases in 2015). More observations and modeling analysis are needed to better characterize the relationship between substorm activity and storm evolution in these two events.

Large interhemispheric asymmetries were observed in high-latitude ground magnetometer data in the 2015 event but not in the 2013 event. We conducted similar analysis as Ganushkina *et al.* [2013] to determine whether these asymmetries could be caused by magnetic field distortions. In particular, we traced magnetic field lines from the Northern Hemisphere NAQ ground magnetometer station to the Southern Hemisphere using IGRF and the Tsyganenko [2002] model to represent the Earth's distorted magnetic field. We used appropriate dipole tilt values and solar wind driving conditions for the each event, examining how distorted the field line was when compared to IGRF (during periods when the station was not on open field lines and the field line tracing could be conducted).

During the period from 1100 to 1500 UT, the Southern Hemisphere foot point is shifted by as much as  $2^\circ$  in latitude and  $-20^\circ$  in longitude in the 2015 event; these shifts are much larger than in the 2013 event and are comparable to some of the largest shifts found in Ganushkina *et al.* [2013]. These large shifts suggest that the Northern and Southern Hemisphere stations are not conjugate during this period, providing an explanation for the different magnetic perturbations observed by Northern and Southern Hemisphere stations from 1100 to 1500 UT. Modeling work is needed to determine which solar wind driving condition(s) played the most important role in distorting the magnetic field at these times, since several parameters can contribute simultaneously. These driving conditions could include solar wind flow direction and speed, dynamic pressure, and IMF. For example, the magnitudes of both IMF  $B_y$  and  $B_z$  were frequently as large as 20 nT between 1100 and 1500 UT in the 2015 event, while IMF  $B_y$  and  $B_z$  both stayed in the range from  $-10$  to 0 nT in the 2013 event.



Substantial interhemispheric asymmetries in ground magnetic perturbations are observed during other periods in the 2015 event, but field line tracing analysis during these periods is either inconclusive or does not indicate major differences between the 2013 and 2015 events. It is possible that the *Tsyganenko* [2002] model does not capture all magnetic field distortions present in the 2015 event. For example, field line tracing analysis based on *Tsyganenko* [2002] suggests Northern and Southern Hemisphere stations are close to magnetically conjugate at 0630 UT, yet global convection maps from SuperDARN at the same time suggest there should be interhemispheric asymmetries in large-scale current systems and the magnetic field (Figure 4). It is also possible that other factors besides magnetic field topology contribute to the observed interhemispheric asymmetries in the high-latitude ground magnetic response. For example, substorm current systems could lead to more disturbed conditions at high latitudes and, thus, interhemispheric asymmetries in ground magnetic perturbations [Tanskanen et al., 2002]. These current systems are more likely to occur during high-speed solar wind streams [Kallio et al., 2000; Tanskanen et al., 2005], and both the 2013 event and 2015 CME storms had elevated solar wind speeds of 650 km/s and 600 km/s, respectively.

The results presented in this study highlight the need for globally distributed observations when characterizing the MI system response. For example, the *AE*, *AL*, and *AU* indices displayed in the fifth panel of Figures 1a and 1b appear qualitatively similar in the first few hours of each event, yet there are major differences between the two events with regard to substorm activity (SCW present in one event and not the other). *AE*, *AL*, and *AU* are also constructed using Northern Hemisphere data that do not capture the interhemispheric differences shown in Figure 3 [e.g., Weygand and Zesta, 2008]. Additionally, the *SYM-H* index displays the expected step-like increase at the beginning of each event that is associated with the intensification of the Chapman-Ferraro currents expected to be strongest on the dayside. However, as shown in Figure 8, strong increases are seen near midnight as well, comparable to or larger than the response seen at noon.

The two CME storm events on 17 March 2013 and 17 March 2015 were unique in that they occurred on the same day of the year at nearly the same time, suggesting global ionospheric conductivity patterns were similar between the two events. Moreover, comparisons between the solar wind driving conditions and ground magnetometer data demonstrate a close relationship between large-scale currents and features in the IMF  $B_z$  and other driving conditions. Thus, large differences in the MI response between the two events can be primarily attributed to variations in the solar wind driver, and the observations presented demonstrate the strong dependence of the MI system response on IMF  $B_z$ . However, additional observations and comparisons with models are needed to fully understand the complicated relationship between the solar wind driver and the dynamics of large-scale current systems occurring during these two events.

## Acknowledgments

The authors would like to thank the support from AGS-1216373, NSF PLR-1543364, and NSF EAR-1520864. We thank the National Space Institute at the Technical University of Denmark (DTU Space) for providing magnetometer data from the Greenland Magnetometer Array. We thank the NASA Space Science Data facility for the OMNI data from the GSFC/SPDF OMNIWeb interface at <http://omniweb.gsfc.nasa.gov>. We thank SPEDAS software for plotting the OMNI data. We thank ground magnetometer data from Intermagnet; USGS, Jeffrey J. Love; 210 Chain, PI K. Yumoto; through the SuperMAG website, PI Jesper W. Gjerloev. The authors acknowledge the use of the "Map Potential Plot" tool hosted by the Virginia Tech SuperDARN group at their website (<http://vt.superdarn.org/tiki-index.php?page=DaViT+Map+Potential+Plot>).

## References

- Birn, J., and M. Hesse (2013), The substorm current wedge in MHD simulations, *J. Geophys. Res. Space Physics*, **118**, 2765–3935, doi:10.1002/jgra.50187.
- Birn, J., and M. Hesse (2014), The substorm current wedge: further insights from MHD simulations, *J. Geophys. Res. Space Physics*, **119**, 3503–3513, doi:10.1002/2014JA019863.
- Chu, X., et al. (2014), Development and validation of inversion technique for substorm current wedge using ground magnetic field data, *J. Geophys. Res. Space Physics*, **119**, 1909–1924, doi:10.1002/2013JA019185.
- Clauer, C. R. (1986), *The Technique of Linear Prediction Filters Applied to Studies of Solar Wind-Magnetosphere Coupling*, edited by Y. Kamide and J. A. Slavin, pp. 39–57, Terra Sci., Tokyo.
- Clauer, C. R. (1994), Solar wind control of high latitude dayside current systems, in *Physical Signatures of Magnetospheric Boundary Layer Processes*, edited by J. A. Holtet and A. Egeland, Kluwer Acad., Dordrecht, Netherlands, doi:10.1007/978-94-011-1052-5\_2.
- Clauer, C. R., and Y. Kamide (1985), *DP 1 and DP 2 current systems for the March 22, 1979 substorms*, *J. Geophys. Res.*, **90**(A2), 1343–1354, doi:10.1029/JA090iA02p01343.
- Clauer, C. R., and R. L. McPherron (1974), Variability of mid-latitude magnetic parameters used to characterize magnetospheric substorms, *J. Geophys. Res.*, **79**(19), 2898–2900, doi:10.1029/JA079i019p02898.
- Clauer, C. R., M. W. Liemohn, J. U. Kozyra, and M. L. Reno (2003), The relationship of storms and substorms determined from mid-latitude ground-based magnetic maps, in *Disturbances in Geospace: The Storm-Substorm Relationship*, edited by A. S. Sharma, Y. Kamide, and G. S. Lakhina, AGU, Washington, D. C., doi: 10.1029/142GM13.
- Clauer, C. R., et al. (2014), An autonomous adaptive low-power instrument platform (AAL-PIP) for remote high-latitude geospace data collection, *Geosci. Instrum. Method. Data Syst.*, **3**, 211–227, doi:10.5194/gi-3-211-2014.
- Ganushkina, N. Y., M. V. Kubyshkina, N. Partamies, and E. Tanskanen (2013), Interhemispheric magnetic conjugacy, *J. Geophys. Res. Space Physics*, **118**, 1049–1061, doi:10.1002/jgra.50137.
- Gjerloev, J. W. (2012), The SuperMAG data processing technique, *J. Geophys. Res.*, **117**, A09213, doi:10.1029/2012JA017683.
- Gonzalez, W. D., J. A. Joselyn, Y. Kamide, H. W. Kroehl, G. Rostoker, B. T. Tsurutani, and V. M. Vasyliunas (1994), What is a geomagnetic storm?, *J. Geophys. Res.*, **99**(A4), 5771–5792, doi:10.1029/93JA02867.
- Kallio, E. I., T. I. Pulkkinen, H. E. J. Koskinen, A. Viljanen, J. A. Slavin, and K. Ogilvie (2000), Loading-unloading processes in the nightside ionosphere, *Geophys. Res. Lett.*, **27**, 1627–1630, doi:10.1029/1999GL003694.

- Kepko, L., R. L. McPherron, O. Amm, S. Apatenkov, W. Baumjohann, J. Birn, M. Lester, R. Nakamura, T. I. Pulkkinen, and V. Sergeev (2015), Substorm current wedge revisited, *Space Sci. Rev.*, *190*, 1–46, doi:10.1007/s11214-014-0124-9.
- King, J. H., and N. E. Papitashvili (2004), Solar wind spatial scales in and comparisons of hourly Wind and ACE plasma and magnetic field data, *J. Geophys. Res.*, *110*, A02209, doi:10.1029/2004JA010804.
- McPherron, R. L., and X. Chu (2016), Relation of the auroral substorm to the substorm current wedge, *Geosci. Lett.*, *3*, 12, doi:10.1186/s40562-016-0044-5.
- Russell, C. T., M. Ginskey, and S. M. Petrinec (1994a), Sudden impulses at low-latitude stations: Steady state response for northward interplanetary magnetic field, *J. Geophys. Res.*, *99*(A1), 253–261, doi:10.1029/93JA02288.
- Russell, C. T., M. Ginskey, and S. M. Petrinec (1994b), Sudden impulses at low latitude stations: Steady state response for southward interplanetary magnetic field, *J. Geophys. Res.*, *99*(A7), 13,403–13,408, doi:10.1029/94JA00549.
- Tanskanen, E. I., T. I. Pulkkinen, H. E. J. Koskinen, and J. A. Slavin (2002), Substorm energy budget near solar minimum and maximum: 1997 and 1999 compared, *J. Geophys. Res.*, *107*(A6), 1086, doi:10.1029/2001JA900153.
- Tanskanen, E. I., J. A. Slavin, D. H. Fairfield, D. G. Sibeck, J. Gjerloev, T. Mukai, A. Ieda, and T. Nagai (2005), Magnetotail response to prolonged southward IMF  $B_z$  intervals: Loading, unloading, and continuous magnetospheric dissipation, *J. Geophys. Res.*, *110*, A03216, doi:10.1029/2004JA010561.
- Tsyganenko, N. A. (2002), A model of the near magnetosphere with a dawn-dusk asymmetry: 2. Parameterization and fitting to observations, *J. Geophys. Res.*, *107*(A8), 1176, doi:10.1029/2001JA000220.
- Weygand, J. M., and E. Zesta (2008), Comparison of auroral electrojet indices in the Northern and Southern Hemispheres, *J. Geophys. Res.*, *113*, A08202, doi:10.1029/2008JA013055.